Polar Radiant Energy in the Far-Infrared Experiment (PREFIRE) Algorithm Theoretical Basis Document (ATBD) for the 2B-FLX data product

Xianglei Huang, Xiuhong Chen, Brian J. Drouin,
Timothy I. Michaels, Erin Hokanson Wagner

R01 release, March/April 2025

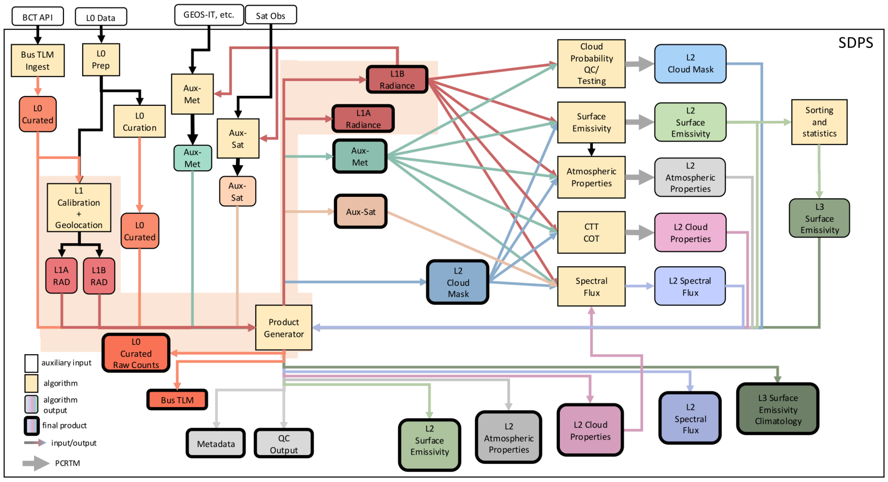

Figure 0.1: PREFIRE algorithm connectivity and flow.

Contents

1 Level-2 Spectral Flux

1.1 Introduction

This algorithm theoretical basis document (ATBD) describes the algorithm used to derive the PREFIRE (Polar Radiant Energy in the Far-InfraRed Experiment) Level-2 spectral flux product (2B-FLX) from the observed PREFIRE spectral radiances. More specifically, this document describes the data, forward modeling tool and algorithm details, and some validation results. We derive both clear-sky and cloudy-sky spectral flux at all available PREFIRE longwave channels ranging from about 5 to 54 μm (PREFIRE channels 6 - 63) over the polar regions.

1.2 Datasets and forward modeling tool

The PREFIRE spectral fluxes are derived from PREFIRE radiances, based on spectral ADMs (Angular Distribution Models) for different sub-scene and surface types. Spectral ADMs were built offline using a forward radiative transfer model (PCRTM version 3.4) and using 6-hourly profiles from the ERA5 (ECMWF Reanalysis version 5). The sub-scene type is also sometimes referred to as a 'discrete interval' in the CERES SSF algorithms (Loeb et al. 2005).

	Sensor	Number of Channels used	Channels used for deriving spectral flux
TIRS1	1	51	6-7 10 -16 19-34 37-50 52-63
	2	47	6-7 10 13-16 19-34 37 39-52 54- 62
	3	45	6-7 10 11 14-16 19 23-34 37-42 44 -60 62-63
	4	52	6-7 10 -16 19-34 37-63
	5	45	6-7 10-16 19-29 31-34 37-49 52 55-57 60- 63
	6	49	6-7 10 -16 19-27 29-34 37-51 53 55-63
	7	45	6-7 10 -16 19-20 22 26-34 37 39-56 58-59 61-63
	8	46	10 12 -16 19-21 23-26 28-34 37-56 58-63
TIRS2	1	46	6-7 10-15 19-34 37 40-47 50-62
	2	51	6-7 10-15 19-34 37-63
	3	21	6-7 10 -16 19 -27 29-31
	4	48	6-7 10-12 14 15 19-28 30-34 37-51 53-63
	5	32	6 -7 10-16 19-34 37-38 40-42 44 53
	6	42	6-7 10-15 19-31 41-43 45-51 53-63
	7	24	6-7 10 13-16 19-29 31-34 38-39
	8	36	6-7 10-16 19-31 38 41-43 46-49 51 53-54 58 61-62

Table 1.1: Number of channels and channels used for deriving PREFIRE spectral flux for each sensor/scene of TIRS1 and TIRS2.

1.2.1 PREFIRE

The PREFIRE mission uses two 6U CubeSats (SAT1 and SAT2), which are in distinct sun-synchronous orbits with an initial altitude of approximately 531 km. The orbit MLTAN (Mean Local Time of the Ascending Node; i.e., the mean local time at which a satellite crosses the equator moving toward the north) for SAT1 is about 03:37, and it is about 08:02 for SAT2. Each CubeSat carries a miniaturized IR spectrometer (Thermal InfraRed Spectrometer; TIRS, or TIRS-PREFIRE), and each instrument has 8 sensors ('scenes') in the cross-track direction, with each of those scenes having 63 detectors ('channels') at $\sim$0.84 μm spectral resolution. PREFIRE measurements are acquired from a near-nadir viewpoint, with the polar regions being the primary area of interest. Channels 8, 9, 17, 18, 35 and 36 are physically masked due to filter boundaries, and so have zero spectral response function. Some additional channels that exhibit high noise or other unreliable operation are also not used — these are different for each of the 16 scenes across both TIRS. Table 1.1 shows the number of channels and specific PREFIRE channels used to derive spectral flux. Spectral fluxes at all TIRS longwave channels (that are not physically masked) are derived based on these filtered radiances at valid channels and corresponding ADMs following Loeb et al., 2005, Huang et al.(2008; 2010; 2014), and Chen et al. (2013).

Figures 1.1, 1.2 and 1.3 show the SRF for each channel and Noise-Equivalent Delta Radiance/Temperature for channels used for deriving spectral flux, respec-

tively, based on PREFIRE SRF files
`PREFIRE_TIRS1_SRF_v12_2023-08-09.nc` and
`PREFIRE_TIRS2_SRF_v12_2023-08-09.nc`

1.2.2 ECMWF reanalysis

The latest European Center for Medium Range Weather Forecasting (ECMWF) ERA5 reanalysis (Hersbach et al. 2020) are used to simulate clear-sky PREFIRE radiance and flux at nadir view. ERA5 is based on the Integrated Forecasting System (IFS) Cy41r2, which was operational in 2016. ERA5 has replaced the popularly used ERA-Interim reanalysis (Dee et al., 2011), and now uses a 12-hourly ten-member ensemble 4D-Var scheme. ERA5 has assimilated myriad historical satellite and *in-situ* observations and forcing from the improved radiation system and sea-surface boundary conditions. The temperature, wind, and humidity in the troposphere are improved compared to ERA-Interim. ERA5 has archived hourly and high spatial resolution data. The vertical pressure levels are still the same as in ERA-Interim (37 levels from the surface to 1 hPa). We only use the 6-hourly profiles of temperature, humidity, as well as surface skin temperature and surface pressure at 1.5^o by 1.5^o grids for simulations. We use four months (January, April, July and October) of data in 2005 for ADM construction.

1.2.3 Forward radiative transfer model

In order to construct ADMs suitable for the PREFIRE mission, a forward radiative transfer model is needed. We use PCRTM (Principal Component-based Radiative Transfer Model) V3.4 for this purpose. PCRTM was developed by Liu et al. (2006). It utilizes the correlations between radiances over different frequencies and thus, compared to line-by-line calculation, greatly reduces the number of monochromatic calculations without significant degradation of the accuracy. Compared with the line-by-line radiative transfer model benchmark calculations, the root-mean-square errors for the PCRTM to calculate an AIRS spectrum is less than 0.4 K (Liu et al., 2006). A recent intercomparison study of fast hyperspectral radiative transfer models for cloudy scenes (Aumann et al., 2018) also confirms the robust performance of the PCRTM compared to other fast radiative transfer models. The PCRTM-based simulator by Chen, Huang, and Liu (2013) is designated to interface the PCRTM with meteorological fields from both climate models and reanalyses in a flexible way and has been used in other published studies (e.g., Bantges et al., 2016; Huang et al., 2014; Pan et al., 2017; Chen et al., 2018).

1.2.4 Synthetic PREFIRE radiance and flux

For clear-sky conditions: The profiles of temperature, humidity and ozone, and surface skin temperature from ECMWF ERA5 are fed into the PCRTM-based radiance simulator to calculate clear-sky spectral radiance at nadir view. Profiles

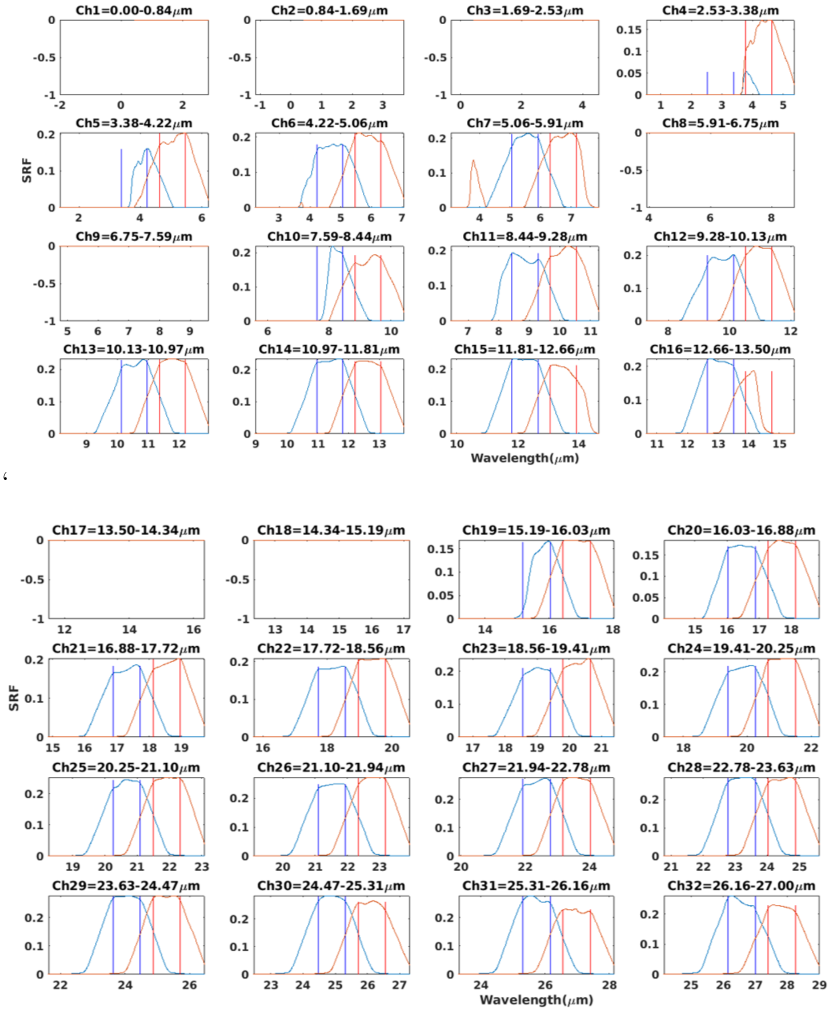

Figure 1.1: Spectral response functions for PREFIRE channels 1-32, slit width = 360 μm. Vertical lines show the lower and upper bounds of each channel. Blue lines are for TIRS1 and red lines are for TIRS2.

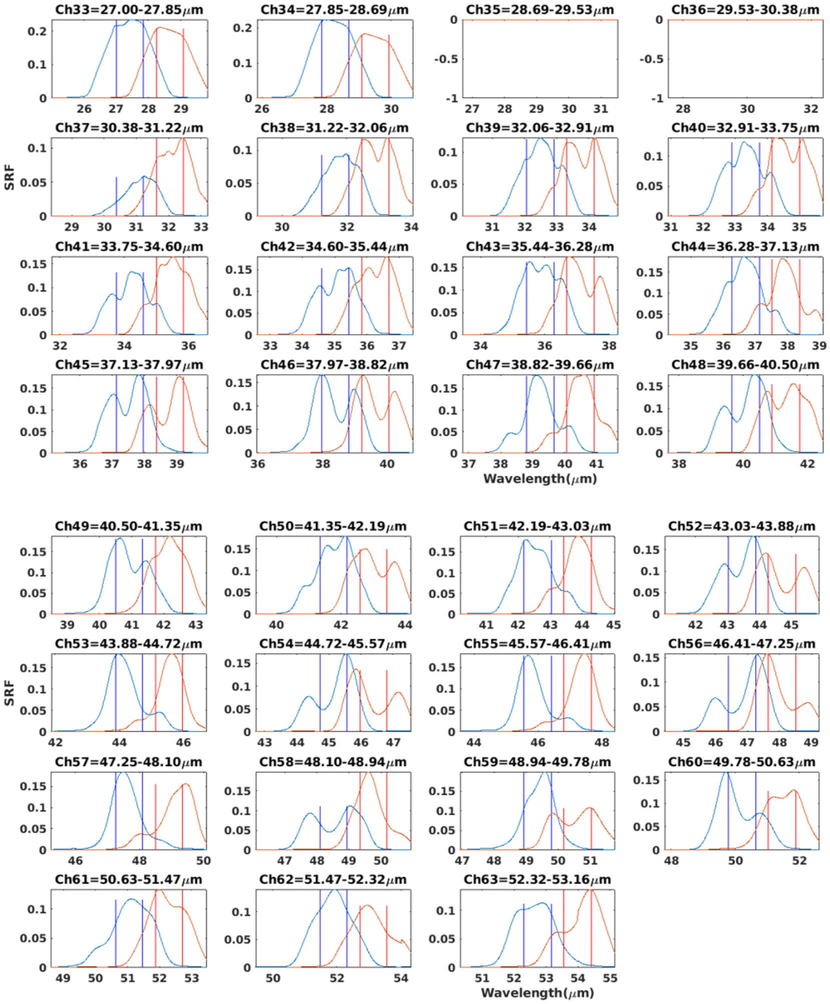

Figure 1.2: Same as Figure 1.1, but for PREFIRE channels 33-63.

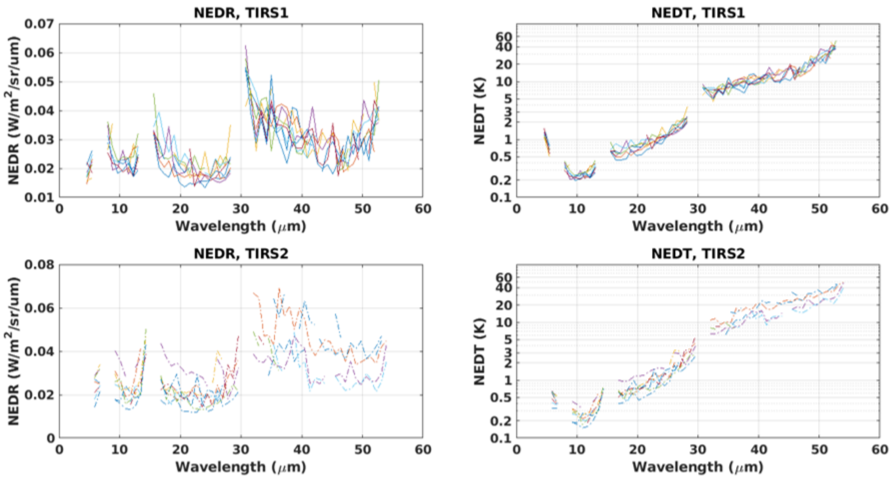

Figure 1.3: (*left*) Noise-Equivalent Delta Radiance (NEdR, 1-sigma radiance noise level) of PREFIRE measurements. (*right*) same as on the left but for Noise-Equivalent Delta Temperature (NEdT) at a temperature of 255 K. Top panels are for TIRS1 and lower panels are for TIRS2. Different colors are for different sensors/scenes.

of CH_4, CO, and N_2O are from standard profiles (McClatchey et al.,1972). The CO_2 vertical profile from McClatchey et al. (1972) is scaled by the CO_2 mixing ratio of the actual month as compiled by National Oceanic and Atmospheric Administration Earth System Research Laboratory. Surface emissivity is from Huang et al. (2016). For sea-ice areas/times, emissivity is a weighted average of water and ice emissivity using sea-ice fraction from ERA5.

For cloudy-sky conditions: The PCRTM also needs cloud phase, cloud optical depth, cloud-particle effective size for each level with clouds. The grid is assumed to be overcast. Clouds above 440 hPa are deemed to be ice clouds, while clouds below 440 hPa are assumed to be water clouds. The effective size of ice cloud particles is parameterized based on cloud temperature (Ou and Liou, 1995), the effective size of water cloud particles is fixed as 20 μm, and the cloud optical depths are calculated from the liquid (Fouquart 1987) and ice water content (Ebert and Curry 1992).

Synthetic PREFIRE radiance is calculated by convolving the PCRTM output at 0.5 cm^{-1} resolution with the spectral response functions of individual PREFIRE channels. Synthetic PREFIRE fluxes are computed using a 2-point (32.333^o, 69.203^o) Gaussian quadrature (Clough et al., 1992), and are just the integration of spectral flux at 0.5 cm^{-1} within each PREFIRE channel (i.e., without convolution with PREFIRE SRFs). The upper panel of Figure 1.4 shows the flux difference between PCRTM using 2-point Gaussian quadrature method and LBLRTM (Line-By-Line Radiative Transfer Model; Clough et al., 1992) using a 3-point Gaussian quadrature method. Fluxes from PCRTM are

1-3 Wm^{-2} larger than fluxes by LBLRTM. The lower two panels of Figure 1.4 show the difference in clear-sky fluxes between 2-point and 3-point Gaussian quadrature. The differences are within -0.1 - 0.6 Wm^{-2}. This suggests that the differences between PCRTM and LBLRTM are mainly from their other radiative transfer assumptions/algorithms, not from Gaussian quadrature.

1.3 Algorithm

Figure 1.5 demonstrates the overall flow of the algorithm. There are three steps in the algorithm: (1) constructing ADMs, $R_v(\theta)$, for all valid PREFIRE channels, and mean synthetic spectral flux (F_n) for each scene type for all channels which includes $F_{PREFIRE}$ for valid PREFIRE channels and $F_{non-PREFIRE}$ for invalid PREFIRE channels), (2) estimating the spectral flux at each PREFIRE valid channel ($F_{PREFIRE}$), and (3) estimating the spectral fluxes at channels with zero SRF or large noise ($F_{non-PREFIRE}$).

1.3.1 Scene type information

Definition of scene or sub-scene type over the polar region (60^o-90^{o}N and 60^o-90^{o}S): The surface types can be categorized into six groups as listed in Table 1.2. They are defined using sea ice fraction, snow depth, and land fraction. The sub-scene type (also called the discrete interval) of a footprint for clear-sky is defined based on surface skin temperature, total column water vapor (precipitable water), and lapse rate (surface skin temperature minus air temperature at (surface pressure - 300 hPa)). The definition of sub-scene types for the clear sky is shown in Table 1.3. The sub-scene type for the cloudy sky is defined based on surface skin temperature, precipitable water, the temperature difference between surface and cloud top, and pseudoradiance (Loeb et al. [2005]; calculated based on cloud optical depth and cloud-top pressure). The cloudy-sky discrete intervals (sub-scene types) of precipitable water, the temperature difference between surface and cloud top, and surface skin temperature are shown in Table 1.4.

Sub-scene type information for ADM construction and PREFIRE flux derivation: For ADM construction, we need sub-scene type information to sort the synthetic PREFIRE radiance and flux into a discrete interval. Sea ice fraction, snow depth, surface skin temperature, total column water vapor and lapse rate are all from ERA5. For PREFIRE flux derivation, given a PREFIRE radiance, we need sub-scene type information to find a proper anisotropic factor in the ADMs. For now, we derive PREFIRE fluxes from synthetic PREFIRE radiances, which are simulated using reanalysis. So, sea ice fraction, snow depth, surface skin temperature, total column water vapor, lapse rate are also from reanalysis. Later, observed PREFIRE radiances can be used, along with sea ice fraction and snow depth can be informed by observation, and surface skin temperature, total column water vapor and lapse rate can be from the ERA5 reanalysis, or PREFIRE retrievals if there are such products. Cloud optical

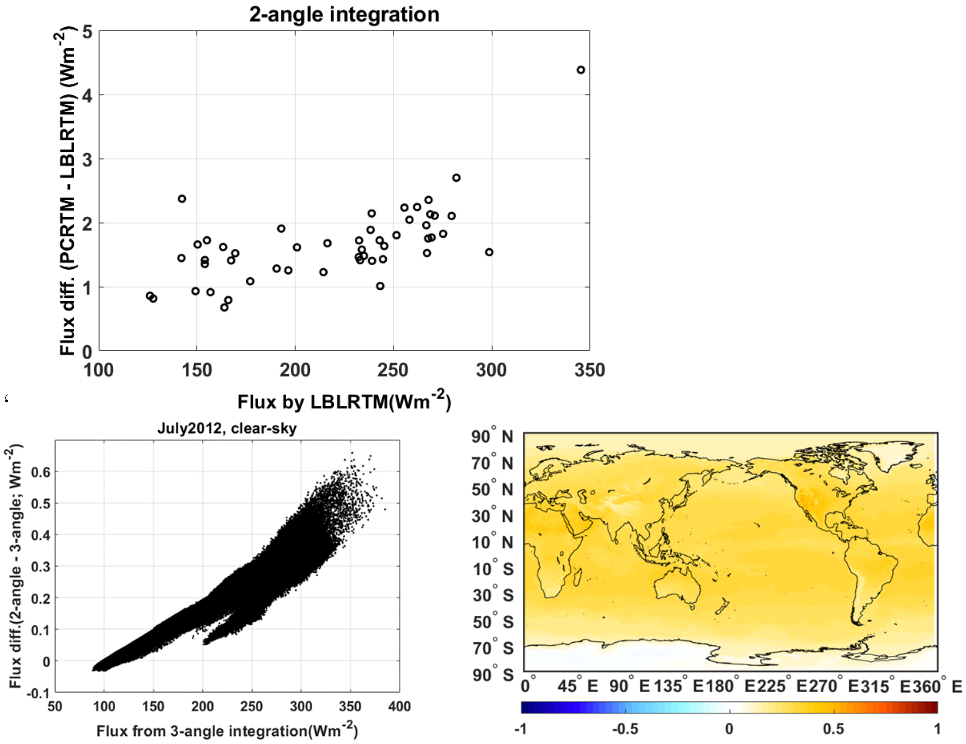

Figure 1.4: (*upper*) Flux difference between PCRTM using a 2-point Gaussian quadrature method and LBLRTM using a 3-point Gaussian quadrature method. 52 profiles from ECMWF, which were used in Liu et al. (2005) for PCRTM validation, are used here for the calculation. (*lower left*) Scatter plot of the difference in clear-sky broadband longwave flux at TOA between 2-point (2-angle) and 3-point (3-angle) Gaussian quadrature method using PCRTM V3.4. (*lower right*) Spatial map of the monthly-mean difference in clear-sky broadband longwave flux at TOA between 2-point and 3-point Gaussian quadrature using PCRTM V3.4. Global mean and RMSE are 0.28 and 0.26 Wm^{-2}, respectively. July 2012 ERA5 data (only 00 UTC for each day) are used for the calculation.

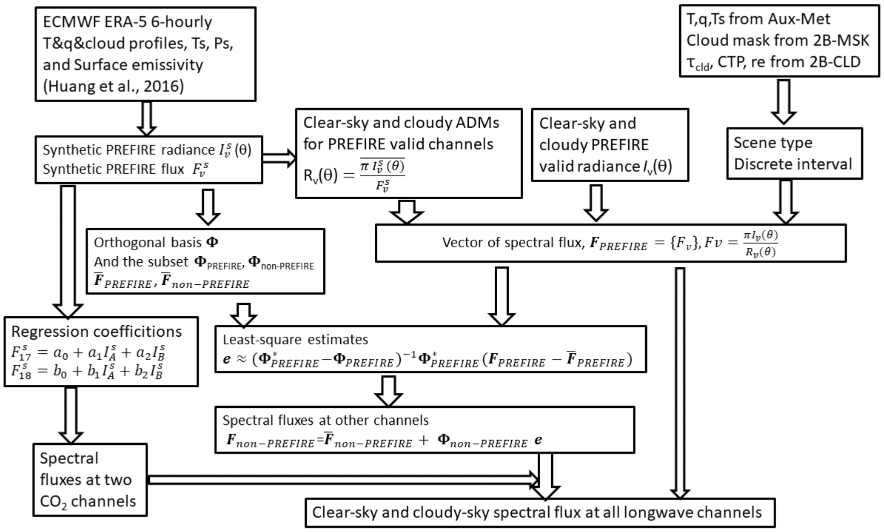

Figure 1.5: Flowchart illustration of the algorithm for deriving spectral fluxes from the PREFIRE radiances.

Surface type	description
Sea ice	sea ice fraction $\geq$95% over the ocean, snow depth <0.001 m
Melted ice	sea ice fraction between 5% and 95% over the ocean, and snow depth <0.001 m
Ocean	sea ice fraction <5% over the ocean, and snow depth <0.001 m
Permanent snow	snow depth $\geq$0.5 m over land (mainly over Antarctica and Greenland)
Fresh snow	0.001 m $\leq$ snow depth < 0.5 m over the land
Non-snow land	snow depth <0.001 m over land

Table 1.2: Surface type classification over the polar regions.

Precipitable water (pw; cm)	lapse rate (ΔT; K)	surface skin temperature (T_s; K)
0-0.5	<-10	<230
0.5-1	-10 - 0	230-250
1-2	0 - 10	250-270
>2	10-20	270-290
	>20	>290

Table 1.3: Definition of clear-sky sub-scene types. Each sub-scene type is defined with respect to different ranges of pw, ΔT, and T_s, which was referred to as a 'discrete interval' in Loeb et al. (2005). ΔT is defined as the lapse rate in the first 300 hPa of the atmosphere above the surface.

Precipitable water (pw; cm)	Surface-cloud temperature difference (ΔT_{sc}; K)	surface skin temperature (T_s; K)
0-0.5	<-15	<230
0.5-1	-15 to 85, every 5 K	230 to 270, every 10 K
1-2	>85	270 to 290, every 5 K
>2		> 290

Table 1.4: Definition of overcast sub-scene types.

depth, cloud-top pressure, and cloud-particle effective radius are retrieved by the PREFIRE cloud properties algorithm (2B-CLD data product).

1.3.2 Spectrally-dependent ADMs

Following Loeb et al. (2005), Huang et al. (2008; 2010; 2014), and Chen et al. (2013), an angular distribution model is needed to convert directional radiance measurement to flux. The central quantity in such conversion is the anisotropic factor, which is defined as

$$R_n(\theta) = \frac{\overline{\pi I_n^s(\theta)}}{F_n^s} \tag{1.1}$$

where $I_n^s(\theta)$ is the synthetic upwelling radiance intensity at TOA for channel n and viewing zenith angle θ. For nadir view, F_n^s is the corresponding synthetic upwelling flux. An overbar denotes the average of all profiles within the same discrete interval as defined in Tables 1.3 and 1.4.

The spectral ADM consists of a set of pre-determined lookup tables of $R_n(\theta)$ for each sub-scene type and for each channel, so it can be used to derive the flux based on Eq. 1.2 using the PREFIRE-measured $I_n(\theta)$.

To construct the spectral ADMs, we used ERA5 fields from four months (January, April, July and October) in 2005. For clear-sky conditions, we build spectral ADMs for each surface type, and more than eight thousand profiles are chosen to construct the spectral ADMs. For cloudy-sky conditions, the spectral

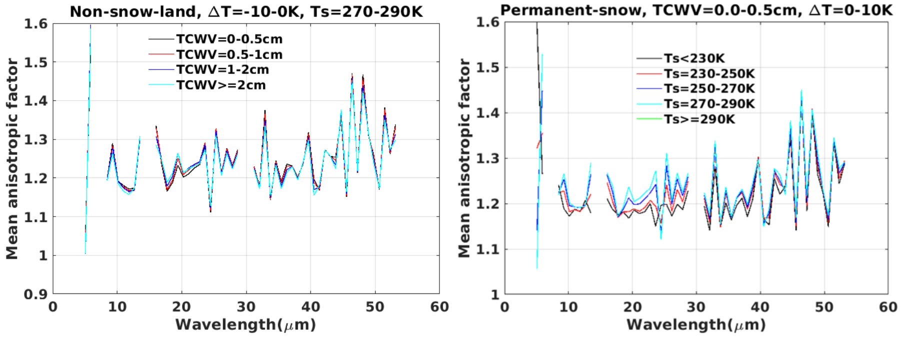

Figure 1.6: (*left*): Mean anisotropic factor for different precipitable water (total column water vapor; TCWV) over a non-snow land surface, (*right*): same as on the left but for different surface skin temperature (T_s) over a permanent ice/snow surface.

ADMs are not dependent on surface type.

Anisotropic factor for different precipitable water and T_s values

Figure 1.6 shows an example of the anisotropic factor for different precipitable water (or total column water vapor; TCWV) and surface skin temperature T_s values. For most PREFIRE channels, $R_n(\theta = 0^o)$ values are within 1.1 and 1.3. $R_n(\theta = 0^o)$ has a small dependence on TCWV except for wavelengths between 16-25 μm. $R_n(\theta = 0^o)$ has a larger dependence on T_s than on TCWV.

Anisotropic factor for different surface types.

Figure 1.7 shows an example of the anisotropic factor for different surface types. The dependence on surface type is obvious for window channels between 8-14 μm.

1.3.3 Estimating spectral longwave fluxes from spectral radiance

The algorithm follows Huang et al. (2008; 2010; 2014), and Chen et al. (2013). For PREFIRE channels with valid radiances, the derivation of spectral flux is straightforward — it merely uses Eq 1.2. With the ADMs, $R_n(\theta)$ (constructed as outlined above) we also need sub-scene type information defined using TCWV, T_s and ΔT to derive spectral flux from PREFIRE spectra. They are either from atmospheric retrievals or from reanalysis. For cloudy-sky conditions, which are determined using the cloud mask product, we also need cloud optical depth, cloud-top pressure, and cloud-particle effective radius. They are from cloud property retrievals.

$$F_n = \frac{\pi I_n(\theta)}{R_n(\theta)} \tag{1.2}$$

$F_{PREFIRE}$=F_n. To obtain spectral fluxes over the entire longwave spectral range, a scheme has to be developed to estimate spectral fluxes at physically-

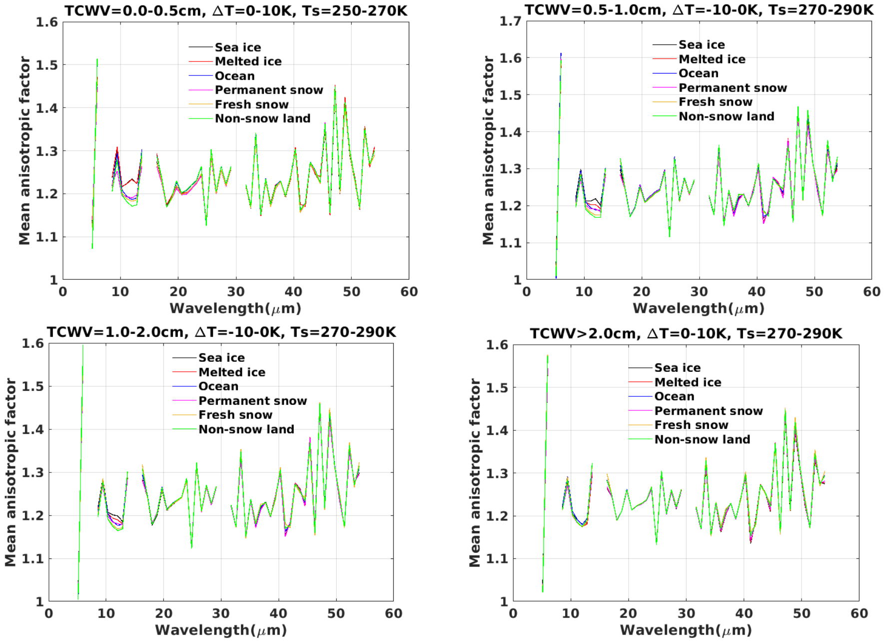
TCWV=0.0-0.5cm, ΔT=0-10K, Ts=250-270K

TCWV=0.5-1.0cm, ΔT=-10-0K, Ts=270-290K

TCWV=1.0-2.0cm, ΔT=-10-0K, Ts=270-290K

TCWV>2.0cm, ΔT=0-10K, Ts=270-290K

Figure 1.7: Mean anisotropic factor for different surface types. Each panel is for a sub-scene type indicated in the title.

masked PREFIRE channels (8, 9, 17, 18, 35, 36) and other channels with large NEdR. A multi-regression scheme based on a Principal Component (PC) analysis is used to obtain the corresponding spectral fluxes. Parameters in the regression scheme are derived based on the ERA5 profiles and synthetic spectra. For every ERA5 profile falling into a given discrete interval, the synthetic spectral fluxes at all channels are computed. Spectral EOF analysis (principal component analysis in the spectral domain) (Haskins et al., 1999; Huang et al., 2003; Huang and Yung, 2005) is then applied to the collection of synthetic spectral fluxes to derive a set of orthogonal basis functions in the frequency domain,

$$F_n^s = \bar{F}_n \sum_{j=1}^{58} e_j \varphi_n^j \tag{1.3}$$

where F_n^s is the synthetic spectral flux at frequency ν_n from one ECWMF profile and $\bar{F}_n$ is the average of all synthetic spectral fluxes at ν_n. The sum spans the total number of channels, $\varphi_n^j (j = 1 - 58)$ are the principal components (unitary vectors) that consist of a complete set of orthogonal bases in the N-dimensional space, and e_j is the projection of $(F_\nu^s - \bar{F}_\nu)$ onto the j^{th} principal component ϕ_ν^j. In practice, it is found that 99.99% variance can be explained by the first 13 or even fewer principal components. Therefore, we only retain the first M principal components that account for 99.99% variance. In the matrix form, it can be written as

$$F^s - \bar{F} \approx [\varphi^1, \varphi^2, \ldots, \varphi^M] \begin{bmatrix} e^1 \\ e^2 \\ \ldots \\ e^M \end{bmatrix} = \Phi e^s \tag{1.4}$$

where F^s, $F \cong \{\bar{F}_{PREFIRE}, \bar{F}_{non-PREFIRE}\}$, $\varphi^1, \varphi^2, \ldots, \varphi^M$ are vectors with a dimension of 58 ($M \ll 58$). Correspondingly, $\Phi = \{\Phi_{PREFIRE}, \Phi_{non-PREFIRE}\}$ is a $58 \times M$ matrix and e_s is an $M \times 1$ vector. Note that the total number of channels is 58. The total number of valid PREFIRE channels is smaller than 58 but still much larger than M. Since Eq. 1.4 holds for all channels, and if we use the subscript 'PREFIRE' to denote a set of valid PREFIRE channels, we still have

$$F_{PREFIRE} - \bar{F}_{PREFIRE} \approx \Phi_{PREFIRE} e \tag{1.5}$$

Note that $F_{PREFIRE}$ could be derived from valid PREFIRE measurements using Eq. 1.2. $\bar{F}_{PREFIRE}$, on the other hand, are the mean spectral fluxes at all PREFIRE channels from the synthetic spectra for each sub-scene type (likewise for ADMs). Eq. 1.5 implies a least-square solution

$$e \approx (\Phi_{PREFIRE} * - \Phi_{PREFIRE})^{-1} \Phi_{PREFIRE} * (F_{PREFIRE} - \bar{F}_{PREFIRE}) \tag{1.6}$$

where $\Phi *$ is the transpose of Φ. In practice, because of $M \ll 58$, $\Phi_{PREFIRE}$ is well-conditioned for every discrete interval and the inversion of $(\Phi *_{PREFIRE}$

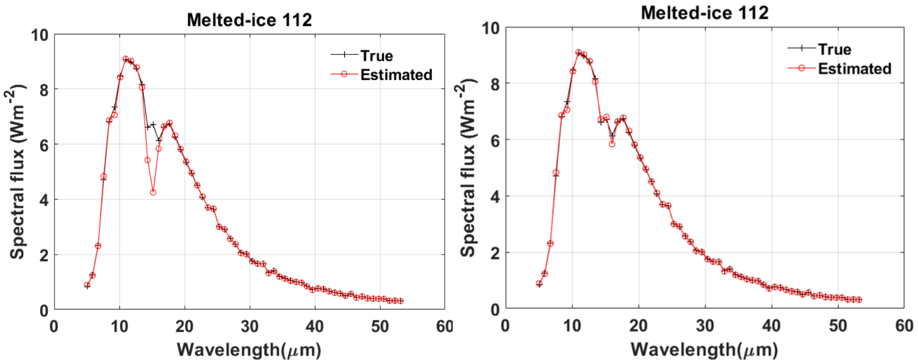

Figure 1.8: (*left*): Comparison of derived spectral flux with true spectral flux over the sea ice surface and for sub-scene type: $0 < \text{TCWV} < 0.5\,\text{cm}$, $\Delta T <$-10 K, and $230\,\text{K} < T_s < 250\,\text{K}$. (*right*): same as at left, but the estimated flux in two CO_2-affected channels are replaced with flux values fit using two-channel radiances.

$\Phi_{PREFIRE}$) is numerically stable. Once e is obtained for every qualified PREFIRE observation, Eq. 1.7 can be used to derive the spectral flux at all PREFIRE channels.

$$F \approx \Phi e + \bar{F} \tag{1.7}$$

where $F = \{F_{PREFIRE}, F_{non-PREFIRE}\}$.

The left panel in Figure 1.8 shows an example of the performance of the algorithm. The derived spectral flux agrees well with true spectral flux except for two channels within/near the CO_2 band. This is largely because those channels have less correlation with other channels. To improve the derived flux at CO_2-affected channels ($n=$ 17, 18), we replace the results with a fitted flux using two-channel (n = 19, 20 for TIRS1 and n = 16, 19 for TIRS2) PREFIRE radiances as follows:

$$F^s_{17} = a_0 + a_1 I^s_A + a_2 I^s_B \tag{1.8}$$

$$F^s_{18} = b_0 + b_1 I^s_A + b_2 I^s_B \tag{1.9}$$

Here, A and B are two valid channels, a_0, a_1, a_2 and b_0, b_1, b_2 are regression coefficients.

Figure 1.9 shows an example of the predicted spectral fluxes at two CO_2-affected channels compared with true fluxes over a sea ice surface. Similar results can be found for other surface types (not shown). Overall, the slope is higher than 0.98 and R^2 is larger than 0.94 for all surface types, regardless of whether noise (data from the left panel of Figure 1.3) is included or not.

Besides the spectral flux at PREFIRE channels, we also provide broadband outgoing longwave radiation (OLR), which covers 5-200 μm. It is an integration of PREFIRE spectral flux from 5 to 54 μm plus an additional band from 54-500 μm which is predicted similarly to channels not covered by PREFIRE.

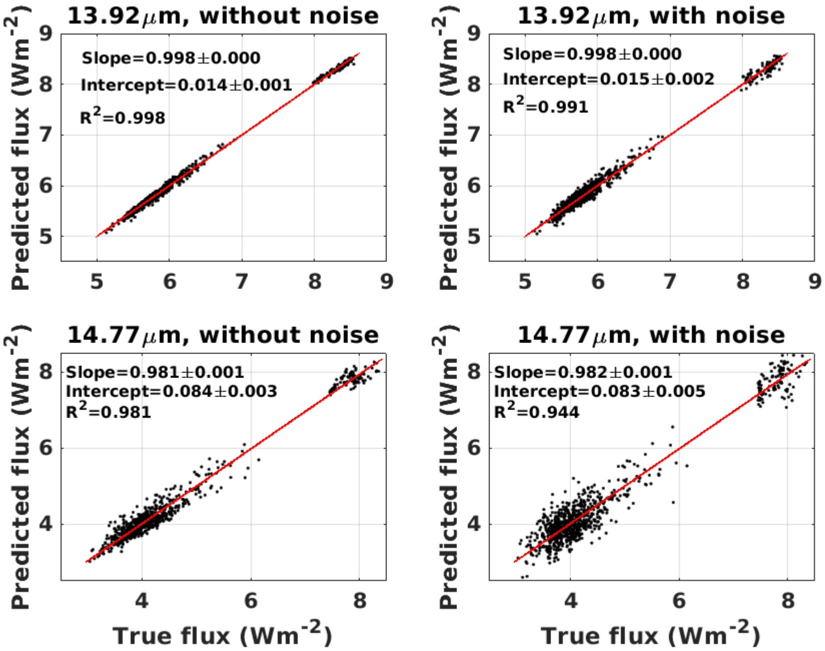

Figure 1.9: Comparison of derived spectral flux with true spectral flux over a sea ice surface for two CO_2-affected PREFIRE channels. Each dot denotes a sub-scene type in 2005. Synthetic PREFIRE radiances and true fluxes are simulated using ERA5 profiles. (*left column*): Predicted fluxes are computed using Eqs 1.8 and 1.9 where the noise of the PREFIRE measurements is not included in I_{19} and I_{20}. (*right column*): Same as in the left column, but the noise of the PREFIRE measurements (data from the left panel of Figure 1.3) is included in I_{19} and I_{20}.

1.4 Validations

1.4.1 Theoretical validation

For theoretical validation, synthetic PREFIRE radiances are used to derive the spectral fluxes and those spectral fluxes are compared with the directly-computed true flux from the PCRTM V3.4. True PREFIRE flux and synthetic PREFIRE radiance are computed using GEOS-FPIT (Goddard Earth Observing System Forward Processing for Instrument Teams) temperature, humidity, and cloud profiles in four months of 2021 (3 days in each month). Synthetic PREFIRE radiances, T and q from the AUX-MET data product (determining sub-scene types for clear-sky conditions), as well as the cloud mask product (2B-MSK; determining clear- or cloudy-sky conditions), the cloud properties product (2B-CLD; determining sub-scene types for cloudy-sky conditions) retrieved from the synthetic PREFIRE radiances, are used by the algorithm to get predicted PREFIRE fluxes. The differences between the spectral fluxes (or the broadband OLR) predicted from the synthetic PREFIRE radiance and the ones directly computed by the PCRTM are examined. This validation strategy lets us assess the whole algorithm without directly assessing the accuracy of spectroscopy and forward modeling, since the PCRTM is used as a surrogate of radiative transfer in the real world.

Figures 1.10 and 1.11 are comparisons (relative difference) between derived spectral fluxes and true (synthetic) fluxes (including both clear- and cloudy-sky conditions) for each sensor/scene of TIRS1 and TIRS2. The largest errors are still from the two CO_2-affected channels (and channels that are not considered valid due to high noise), and these two channels have less correlation with other valid channels.

Figures 1.12 and 1.13 are histograms of the difference between predicted OLR and true (synthetic) OLR (including both clear- and cloudy-sky conditions) for each sensor/scene of TIRS1 and TIRS2. OLR is the integration of spectral flux over the entire relevant longwave range. Overall, the OLR differences are within ± 5 Wm^2.

Table 1.5 summarizes the relative differences between predicted and true spectral flux at all PREFIRE channels. Table 1.6 summarizes the relative difference between predicted and true OLR values. The median errors are very close to 0% for both TIRS1 and TIRS2. The RMSE errors of TIRS2 are generally larger than those of TIRS1, which is primarily due to the spectral shifts of two physically-masked channels near $15\,\mu\mathrm{m}$ for TIRS2 compared to TIRS1.

1.4.2 Validation using observations

Relevant validation using actual PREFIRE in-orbit observations has not yet been completed.

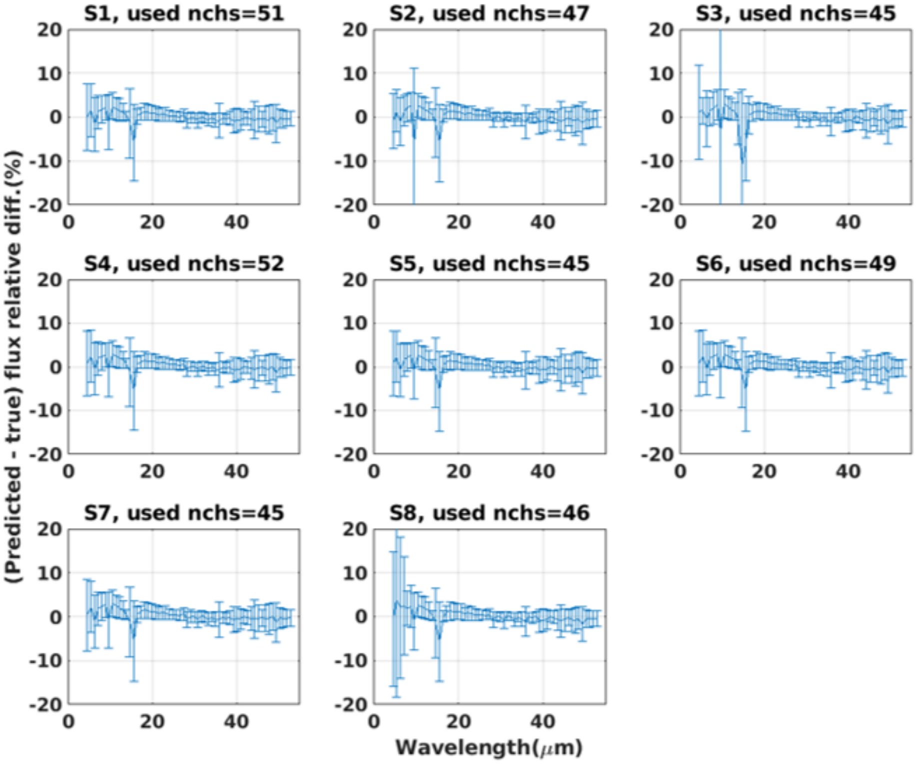

Figure 1.10: Relative difference between predicted and true spectral flux for all PREFIRE longwave channels, and for each sensor/scene of TIRS1. The sensor number and number of channels used for deriving the longwave flux shown are indicated in the title. All cases are from the polar regions.

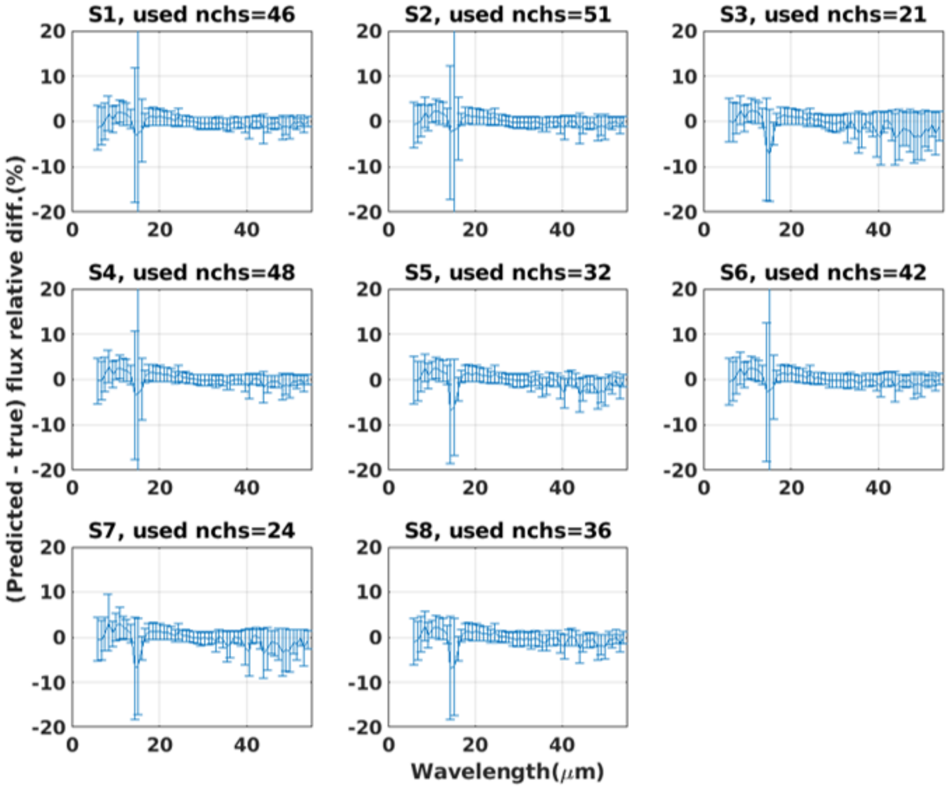

Figure 1.11: Same as Figure 1.10, but for the 8 sensors/scenes of TIRS2.

Sensor	TIRS1 Sim Performance			TIRS1 Error Delta	TIRS2 Sim Performance			TIRS2 Error Delta
	5^{th}	95^{th}	median		5^{th}	95^{th}	median	
1	-6.3	4.7	-0.1	13.4	-38.5	4.0	-0.2	22.6
2	-6.9	4.7	0.1	13.6	-37.8	4.2	-0.1	22.6
3	-8.3	4.9	0.1	14.1	-28.9	4.5	-0.3	22.6
4	-6.2	5.0	0.2	13.4	-38.2	4.3	0.0	22.6
5	-6.6	5.1	0.1	13.5	-24.8	4.0	-0.2	22.4
6	-6.4	5.0	0.2	13.4	-41.6	4.3	-0.0	22.7
7	-6.5	5.0	0.1	13.5	-26.4	4.5	-0.2	22.5
8	-7.5	5.3	-0.0	14.0	-25.8	3.9	-0.3	22.4
Aggregate	-6.7	5.0	0.1	13.6	-33.1	4.2	-0.2	22.6

Table 1.5: 5^{th}, 95^{th} percentile, median value, and error Delta (root mean square error) of the relative difference (%) between predicted and true spectral flux for TIRS1 and TIRS2. Aggregate values are from the combination of all 8 sensors/scenes.

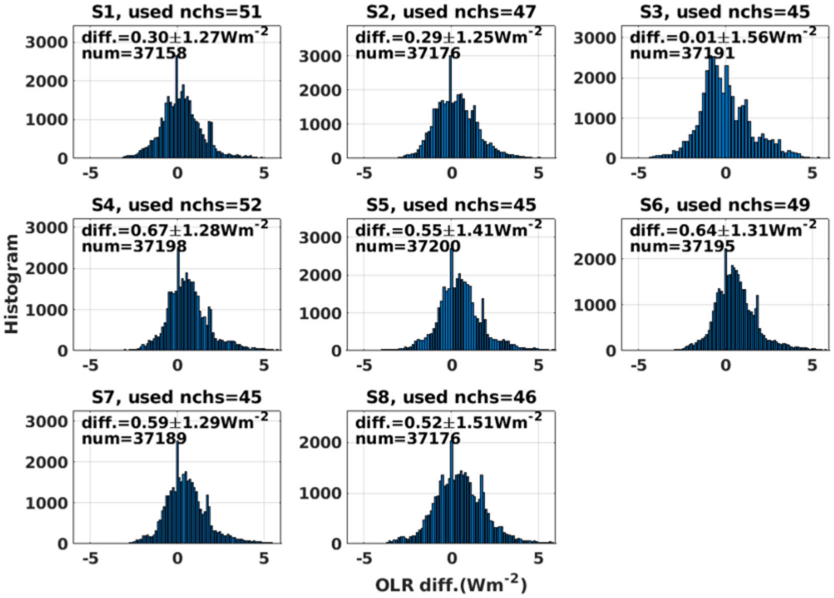

Figure 1.12: Histogram of OLR difference between prediction and truth for the 8 sensors/scenes of TIRS1. The mean, standard deviation, and number of cases are shown on each panel. All cases are from the polar regions.

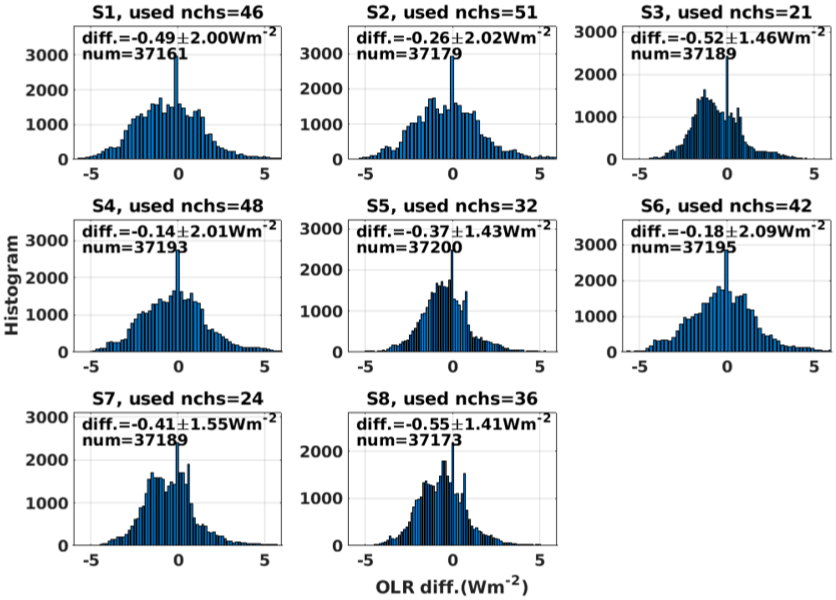

Figure 1.13: Same as Figure 1.12, but for the 8 sensors of TIRS2.

Sensor	TIRS1 Sim Performance			TIRS1 Error Delta	TIRS2 Sim Performance			TIRS2 Error Delta
	5^{th}	95^{th}	median		5^{th}	95^{th}	median	
1	-1.6	2.3	0.2	1.3	-3.5	2.7	-0.5	2.1
2	-1.6	2.5	0.2	1.3	-3.3	3.2	-0.2	2.0
3	-2.2	2.9	-0.2	1.6	-2.7	2.2	-0.7	1.6
4	-1.2	3.1	0.5	1.4	-3.1	3.2	-0.1	2.0
5	-1.6	3.1	0.4	1.5	-2.6	2.2	-0.4	1.5
6	-1.2	3.0	0.5	1.5	-3.4	3.1	-0.1	2.1
7	-1.2	3.0	0.5	1.4	-2.7	2.2	-0.4	1.6
8	-1.7	3.0	0.4	1.6	-2.7	1.9	-0.5	1.5
Aggregate	-1.6	2.9	0.3	1.5	-3.0	2.6	-0.4	1.8

Table 1.6: Same as Table 1.5, but for the relative difference (%) of predicted and true OLR for TIRS1 and TIRS2.

1.5 References

Aumann, H. H., et al., 2018: Evaluation of radiative transfer models with clouds. Journal of Geophysical Research: Atmospheres, 123, 6142–6157.
https://doi.org/10.1029/2017JD28073.

Bantges, R., H. Brindley, X. H. Chen, X. L. Huang, J. Harries, & J. Murray, 2016: On the detection of robust multi-decadal changes in the Earth's outgoing longwave radiation spectrum. J. Climate, 29(13), 4939–4947.
https://doi.org/10.1175/JCLI-D-15-0713.1.

Chen, X. H., X. L. Huang, and X. Liu, 2013: Non-negligible effects of cloud vertical overlapping assumptions on longwave spectral fingerprinting studies. Journal of Geophysical Research: Atmospheres, 118, 7309-7320.
https://doi.org/10.1002/jgrd.50562.

Chen, X. H., X. L. Huang, N. G. Loeb, H. L. Wei, 2013: Comparisons of clear-sky outgoing far-IR flux inferred from satellite observations and computed from three most recent reanalysis products. J. Climate, 26(2), 478-494,
doi:10.1175/JCLI-D-12-00212.1.

Chen, X. H., X. L. Huang, X. Q. Dong, B. K. Xi, E. Dolinar, N. Loeb, S. Kato, P, Stackhouse, M. Bosilovich, 2018: Using AIRS and ARM SGP clear-sky observations to evaluate meteorological reanalyses: a hyperspectral radiance closure approach. JGR-Atmospheres, 123 (20), 11720-11734, 10.1029/2018JD028850.

Clough et al., 1992: Line-by-Line Calculations of Atmospheric Fluxes and Cooling Rates' Application to Water Vapor. Journal of Geophysical Research:

Atmospheres,15,761-15,785, 1992.

Dee, D. P., et al., 2011: The ERA-Interim reanalysis: Configuration and performance of the data assimilation system. Quarterly Journal of the Royal Meteorological Society, 137(656), 553–597.
https://doi.org/10.1002/qj.828. Haskins, R., et al., 1999: Radiance covariance and climate models. J. Climate, 12, 1409–1422.

Ebert, E. E., and Curry, J. A. 1992: A parametrization of ice cloud optical properties for climate models, Journal of Geophysical Research: Atmospheres, 97, 3831–3836.

Fouquart, Y. 1987: Radiative transfer in climate models, in Physically Based Modelling and Simulation of Climate and Climate Changes, edited by M. E. Schlesinger, pp. 223–284, Kluwer Acad., Norwell, Mass.

Hersbach, H. et al., 2020: The ERA5 global reanalysis. Quarterly Journal of the Royal Meteorological Society, 146,
https://doi.org/10.1002/qj.3803.

Huang, X. L., and Y. L. Yung, 2005: Spatial and spectral variability of the outgoing thermal IR spectra from AIRS: A case study of July 2003. J. Geophys. Res., 110, D12102, doi:10.1029/2004JD005530.

Huang, X. L., J. J. Liu, and Y. L. Yung, 2003: Analysis of thermal emission spectrometer data using spectral EOF and tri-spectral methods. Icarus, 165, 301–314, doi:10.1016/S0019-1035(03)00206-9.

Huang, X. L., N. G. Loeb, and W. Z. Yang, 2010: Spectrally resolved fluxes derived from collocated AIRS and CERES measurements and their application in model evaluation: 2. cloudy sky and band-by-band cloud radiative forcing over the tropical oceans. J. Geophys. Res. Atmos, 115, D21101, doi:10.1029/2010JD013932.

Huang, X. L., W. Z. Yang, N. G. Loeb, and V. Ramaswamy, 2008: Spectrally resolved fluxes derived from collocated AIRS and CERES measurements and their application in model evaluation: 1. clear sky over the tropical oceans. J. Geophys. Res. Atmos, 113, D09110, doi: 10.1029/2007JD009219.

Huang, X. L., X.H. Chen, D. K. Zhou, X. Liu, 2016:An observationally based global band-by-band surface emissivity dataset for climate and weather simulations. Journal of the Atmospheric Sciences, 73, 3541-3555, doi:10.1175/JAS-D-15-0355.1.

Huang, X. L., X. H. Chen, G. L. Potter, L. Oreopoulos, J. N.S. Cole, D.M. Lee, N. G. Loeb, 2014: A global climatology of outgoing longwave spectral cloud radiative effect and associated effective cloud properties. J. Climate, 27, 7475-7492, doi:10.1175/JCLI-D-13-00663.1.

Huang, X. L., X. H. Chen, B. J. Soden, & X. Liu, 2014: The spectral dimension of longwave feedbacks in the CMIP3 and CMIP5 experiments. Geophysical Research Letters, 41, 7830–7837.
https://doi.org/10.1002/2014GL061938.

Liu, X., W. L. Smith, D. K. Zhou, & A., Larar, 2006: Principal component-based radiative transfer model for hyperspectral sensors: Theoretical concept. Applied Optics, 45(1), 201–209.
https://doi.org/10.1364/AO.45.000201.

Loeb, N. G., S. Kato, K. Loukachine, and N. Manalo-Smith, 2005: Angular distribution models for top-of-atmosphere radiative flux estimation from the Clouds and the Earth's Radiant Energy System instrument on the Terra satellite. Part I: Methodology. J. Atmos. Oceanic Technol., 22, 338–351, doi:10.1175/JTECH1712.1.

Loveland, T. R., and Coauthors, 2000: Development of a global land cover characteristics database and IGBP DISCover from 1 km AVHRR data. Int. J. Remote Sensing, 21, 1303–1330.

McClatchey, R., R. Fenn, J. Selby, F. Volz, and J. Garing, 1972: Optical properties of the atmosphere, Tech. Rep. AFCRL-72-0497, AFGL (OPI), Hanscom AFB, MA 01731.

Ou, S.-C., and K.-N. Liou 1995: Ice microphysics and climatic temperature feedback. Atmos. Res., 35, 127–138.

Pan, F., X. L. Huang, S. S. Leroy, P. Lin, L. L. Strow, Y. Ming, & V. Ramaswamy, (2017). The stratospheric changes inferred from 10 years of AIRS and AMSU-A radiances. J. Climate, 30(15), 6005–6016.
https://doi.org/10.1175/JCLI-D-17-0037.1.

2 Appendix

2.1 Table of variables and symbols

$\mathbf{A}$	averaging kernel matrix
α	angular resolution
β	azimuth angle
B	blackbody radiance
BW	spectral bandwidth
χ	convergence criterion
c	speed of light, cost function
CED	Cloud particle Effective Diameter
COD	Cloud Optical Depth
CTP	Cloud Top Pressure
CWP	Cloud Water Path
d	degree of freedom
ε	emissivity
ϵ	noise, error
ϕ	longitude
E	irradiance
F	flux
f	focal length
$\mathcal{F}$	function
γ	*a priori* weight
G	gravitational constant
g	gain
H	height
h	Planck's constant
I	radiance
IC	Information Content
IWC	Ice Water Content
IWP	Ice Water Path
j	counter
k	Boltzmann's constant, unknown
$\mathbf{K}$	Jacobian
λ	wavelength, Marquardt-Levenberg parameter
l	distance
L	radiance
LTS	Lower Tropospheric Stability
LWC	Liquid Water Content
LWP	Liquid Water Path
M	counter, mass
m	number of along-track frames
$\mathcal{M}$	matrix

N	counter
n	channel
$\mathcal{N}$	normal distribution
ν	frequency
NEdT	Noise-Equivalent delta Temperature
o	offset
Ω	solid angle
p	pressure
P	probability
PWV	Precipitable Water Vapor
Q	water vapor
ρ	reflection coefficient
R	radius, resistance, cost-function change
$\Re$	response function
$\wp$	responsivity
σ_B	Stefan-Boltzmann constant
$\mathbb{S}$	signal level in digitized counts
S	covariance
SI	Segmentation Index
SNR	Signal-to-Noise Ratio
SRF	Spectral Response Function
θ	latitude, potential temperature, polar coordinate angle
τ	transmission, optical depth
T	temperature
TR	Training Radiances
TREM	TRaining Eigenvector Matrices
t	time
ϕ	polar coordinate angle
V	voltage
v	velocity
x, y, z	position coordinates
z	convergence, standard deviation of scaled differences
$\mathbf{x}$	state vector
X	focal plane position
$\mathbf{y}$	measurement vector
Y	focal plane position
ζ	incidence angle

Table 2.1: Table of variables and symbols.

2.2 Abbreviations and acronyms

ADM	Angular Distribution Model
AIRS	Atmospheric Infrared Sounder
ATBD	Algorithm Theoretical Basis Document
CERES	Clouds and the Earth's Radiant Energy System
DEM	Digital Elevation Model
DOF	Degree of Freedom
ECI	Earth-Centered Inertial
ECMWF	European Centre for Medium-Range Weather Forecasts
EOF	Empirical Orthogonal Function
FIR	Far-InfraRed
FOV	Field Of View
FPA	Focal Plane Array
FWHM	Full Width at Half Maximum
GEOS-IT	Goddard Earth Observing System for Instrument Teams
GMAO	Global Modelling and Assimilation Office
IFOV	Instantaneous Field Of View
IFS	Integrated Forecasting System
LW	Longwave
MIR	Mid-InfraRed
NASA	National Aeronautics and Space Administration
NEP	Noise Equivalent Power
NEdR	Noise Equivalent delta spectral Radiance
OE	Optimal Estimation
OLR	Outgoing Longwave Radiation
PCRTM	Principal Component-based Radiative Transfer Model
PREFIRE	Polar Radiant Energy in the Far-InfraRed Experiment
ROIC	Read-Out Integrated Circuit
RMSE	Root Mean Square Error
SDPS	Science Data Processing System
SSF	Single Scanner Footprint
SRF	Spectral Response Function
TCWV	Total Column Water Vapor
TIRS	(TIRS-PREFIRE) Thermal InfraRed Spectrometer
TIRS1	Thermal InfraRed Spectrometer on PREFIRE-SAT1
TIRS2	Thermal InfraRed Spectrometer on PREFIRE-SAT2
TOA	Top of Atmosphere
UTC	Coordinated Universal Time
VZA	Viewing Zenith Angle
WV	Wavelength

Table 2.2: Abbreviations and acronyms.

2.3 Figure listing with links

Table 2.3: List of Figures in this ATBD.